Chapter 7

Probe-sample distance control

In near-field optical microcopy, a local probe has to be brought into close proximity to the sample surface. Typically, the probe-sample distance is required to be smaller than the size of lateral field confinement and thus smaller than the spatial resolution to be achieved. For example, an optical probe with a lateral light confinement of $\sim$50 nm demands a probe-sample distance of $\leq$5 nm to take full advantage of the light confinement (c.f. Section 4.6). As in other types of scanning probe techniques, an active feedback loop is required to maintain a constant distance during the scanning process. However, the successful implementation of a feedback loop requires a sufficiently short-ranged interaction between optical probe and sample. The dependence of this interaction on probe-sample distance should be monotonous in order to ensure a unique distance assignment. A typical block-diagram of a feedback loop applied to scanning probe microscopy is shown in Fig. 7.1. A piezoelectric element

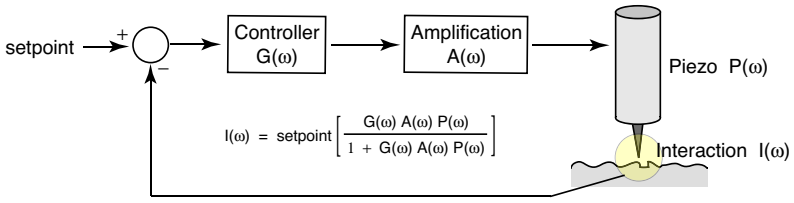

Figure 7.1: Characteristic diagram of a feedback loop employed in scanning probe microscopy. Ideally, the measured interaction signal corresponds to the externally defined setpoint. The speed and stability of the feedback loop depend on the parameters of the controller $G(\omega)$.

$P(\omega)$ is used to transform an electric signal into a displacement whereas the interaction measurement $I(\omega)$ takes care of the reverse transformation. The controller $G(\omega)$ is used to optimize the speed of the feedback loop and to ensure stability according to well-established design rules. Most commonly, a so-called PI controller is used which is a combination of a proportional gain (P) and an integrator stage (I).

Using the (near-field) optical signal itself as a distance-dependent feedback signal seems to be an attractive solution at the first glance. However, it turns out that (1) in presence of a sample of unknown and inhomogeneous composition, unpredictable variations in the near-field distribution give rise to non-monotonous distance dependence. Such behavior inevitably leads to frequent probe damage. (2) The near-field signal is often small and masked by far-field contributions, and (3) the decay length of the near fields of optical probes is often too long to serve as a reliable measure for distance changes on the nanometer scale. For these reasons, usually an auxiliary distance feedback is required for the operation of optical probes.

Standard scanning probe techniques basically employ two different types of interactions, i.e. electron tunnelling (STM) [1] and attractive or repulsive interaction forces normal and lateral to the surface (AFM) [2]. Electron tunnelling requires a conductive sample. This is a strong limitation in view of the spectroscopic capabilities of optical microscopy that are lost by covering the sample with a metallic layer. Therefore, near-field optical microscopy most commonly employs feedback loops based on short-range interaction forces. In the past, several cantilever-type probes have been developed. This implementation is appealing because such probes could be used in standard commercial AFMs. However, for reasons of reliability and simplicity of implementation, the most wide-spread probe-sample distance control in near-field optics is based on the measurement of lateral shear or friction forces.

Before we go into more details an important note has to be made. In standard commercial AFMs and STMs the short-ranged interaction used for feedback is also the physical quantity of interest. This is not the case in near-field optical microscopy with auxiliary feedback. The use of an auxiliary feedback mechanism inherently bears the danger of introducing artifactual changes in the optical signal not related to the optical properties of the sample but to changes in the probe-sample distance induced by the auxiliary feedback. This is of major importance if the apex of the optical probe and the force sensor do not coincide. These problems and possible solutions are discussed in detail in the final section of this chapter and also in Refs. [3, 4].

7.1 Shear-force methods

It was found that the vibration of a probe in a direction parallel to the sample surface is influenced by the proximity of the sample. Typically, the probe is oscillated at the

resonance frequency of its mechanical support (vertical beam, tuning fork) and the amplitude, phase, and/or frequency of the oscillation are measured as a function of the probe-sample distance. The interaction range is 1 to 100 nm, depending on the type of probe and the particular implementation. The nature of this so-called shear-force is still under debate. It is accepted that at ambient conditions the effect originates from the interaction with a surface humidity layer. However, the shear-force can even be measured in high vacuum conditions and at ultralow temperatures [5, 6] and thus there must be more fundamental interaction mechanisms such as electromagnetic friction [7]. Whatever the origin, the distance dependent shear-force is an ideal feedback signal for maintaining the near-field probe in close proximity to the sample surface.

7.1.1 Optical fibers as resonating beams

The simplest type of shear-force sensor is the oscillating beam. It represents a clamped short piece of a glass fiber or a metal rod with a tip at its end. The resonance frequency of the beam depicted in Fig. 7.2 scales with the square of its free length L. This scaling holds for any type of cantilever fixed at one end. The fundamental resonance frequency of an oscillating beam with circular cross-section is calculated as[8]

$$\omega_o \;=\; 1.76\sqrt{\frac{E}{\rho}}\,\frac{R}{L^2}\;, \tag{7.1}$$

where E is Young's modulus, ρ the specific mass density, R the radius of the beam, and L the length of the beam. For the example of an optical fiber with radius $R{=}125\,\mu m$ and length $L{=}3\,mm$ we obtain $f_o = \omega_o/(2\pi) \approx 20\ kHz$. A typical quality factor of such a probe in air is about 150. Changing the length of the fiber will strongly change

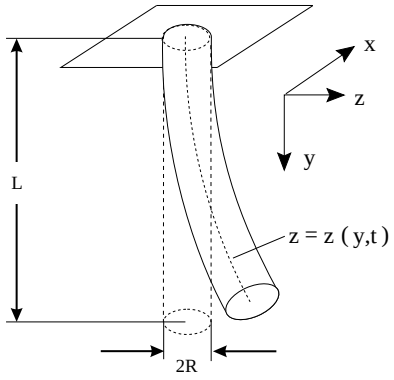

Figure 7.2: Sketch of a quartz beam of length L used to calculate the resonances of an oscillating fiber probe.

the resonance frequency according to Eq. 7.1.

When the end of the beam starts to interact with a surface the resonance frequency will shift and the oscillation amplitude will drop. This situation is depicted in Fig. 7.3(a,b) for a beam that is externally driven at a variable frequency ω. Amplitude and phase of the beam oscillation are shown for two different distances (d) between the beam-end and the sample surface. The amount of shift depends critically on the interaction area, i.e. the diameter of the beam. Fig. 7.3(c,d) show the amplitude shift and the phase shift, respectively, as a function of the distance d for the case that the beam is driven at its original resonance frequency $\omega = \omega_o$. The distance-range over which the amplitude and phase vary depends on the diameter of the beam, i.e. the tip diameter in case of a sharp near-field probe. Because of the monotonous behavior of the curves in Fig. 7.3(a,b), amplitude and phase are well-suited feedback signals. Usually they are detected with a lock-in amplifier. As will be discussed later on, in high-sensitivity applications that require a high Q-factor (narrow resonances) it is favorable of not driving the beam at a fixed frequency ω. Instead, with a self-oscillating circuit the beam can be vibrated at its natural resonance frequency [9]. As illustrated in Fig. 7.3(a,b), the resonance frequency shifts as the oscillating beam-end

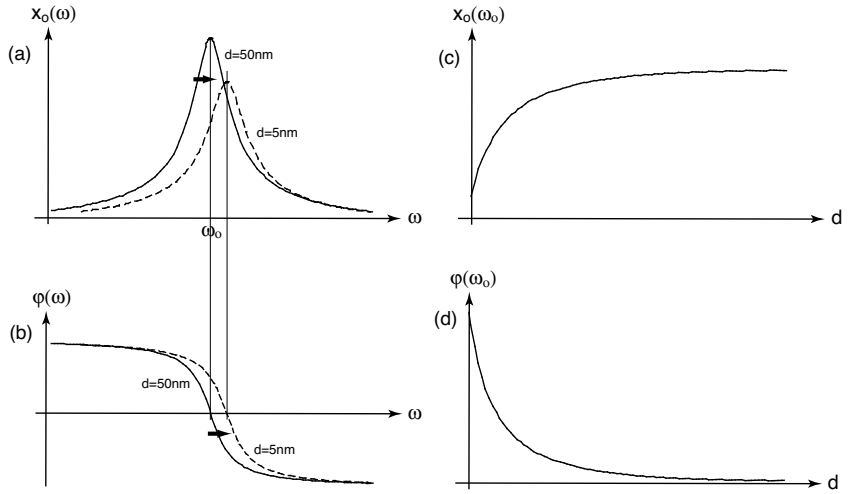

Figure 7.3: Resonance of a vibrating beam. Amplitude (a) and phase (b) of a beam driven at a frequency ω. As the beam-end starts to interact with a sample surface, the resonance shifts and the amplitude drops. (c,d) show the amplitude and phase at frequency $\omega = \omega_o$ as a function of the distance between beam-end (tip) and surface. The distance-range over which the amplitude and phase vary depends on the interaction area (tip sharpness).

is approached towards the sample surface and thus the frequency shift $\Delta\omega$ can be used as an alternative feedback signal. A further possibility is to use the Q-factor of the resonance as a feedback signal which would correspond to operation in constant-dissipation mode. Which type of feedback signal to use depends on the particular type of experiment. In general, complementary information about the probe-sample interaction can be accessed by recording amplitude, phase, frequency shift, and Q-factor simultaneously as auxiliary signals.

There are several ways of directly detecting the vibration of an oscillating optical probe. The simplest method [see Fig. 7.4 (a)] is to project the light emitted or scattered from an optical probe onto a suitably positioned aperture and to detect the transmitted light intensity. The modulation amplitude of the optical signal at the dither frequency of the tip will reflect the amplitude and phase of the tip oscillation [10]. In a near-field optical microscope, this method interferes with the detection path of the optical signal and thus can be influenced by the optical properties of the sample. Therefore, alternative optical detection schemes were developed which employ a beam path perpendicular to the optical detection path of the microscope. An auxiliary laser can be pointed to the probe and the resulting diffraction pattern is detected by a split photodiode [see Fig. 7.4 (b)]. This scheme works well but it can suffer from mode hopping of the laser diode or drifts in the mechanical setup leading to changes in the (interference) pattern on the photodiode. Also, it is clear that the

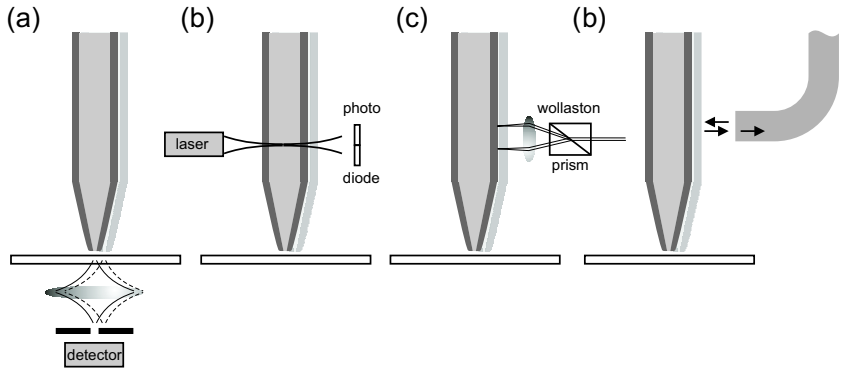

Figure 7.4: Different methods for the direct detection of the oscillation of an optical probe. (a) Aperture detection scheme: the light emitted or scattered by the probe is focused on to a pinhole. The detected light is modulated at the mechanical resonance frequency of the probe. (b) Laser deflection scheme: a infrared diode laser is scattered or deflected by the fiber probe. The resulting oscillating fringe pattern is directed to a split photodiode. (c) Differential interferometry using a Wollaston prism. (d) Interferometry using a fiber optic interferometer.

motion sensed along the shaft of the probe is not identical to the motion of the tip apex itself. This can be a problem if higher-order oscillation modes of the probe are excited. The same arguments may apply to interferometric detection schemes, e.g. using differential interferometry [11] or a fiber interferometer [12, 13] [see Fig. 7.4 (c)]. The latter methods are, however, very sensitive and can detect amplitudes well below 10 **r**A. However, the direct optical detection of probe oscillation is not widely employed anymore because indirect methods, using quartz or piezoceramic sensors, have proven to be favorable in terms of sensitivity and simplicity of implementation.

7.1.2 Tuning fork sensors

When using optical methods to detect the optical probes lateral vibration the danger exists that the optical detection interferes with the detection of a generally weak near-field optical signal. This is especially important when spectroscopic experiments are performed or photosensitive samples are investigated. Therefore, alternative sensing methods were developed that do not employ light. Many of them are based on measuring changes in the admittance of piezoelectric devices that are related to a change in the resonant behavior upon interaction with the sample of the piezoelectric device itself or an optical probe attached. The piezoelectric element can be a piezo plate [14] or tube [15]. However, the most successful and widespread method of shear-force

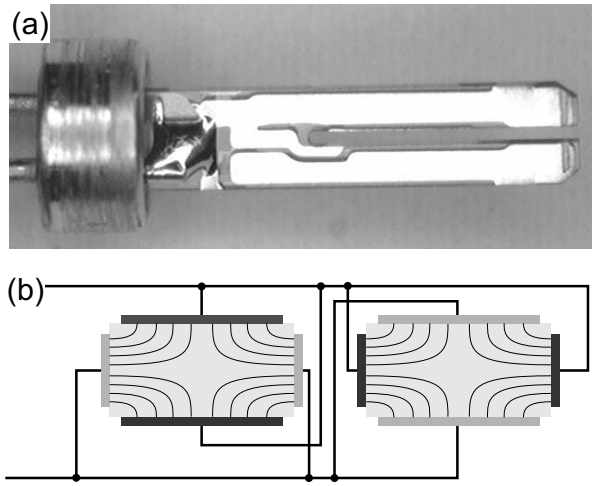

Figure 7.5: Quartz tuning fork: (a) Enlarged photograph. Dimensions of the quartz element shown are 5870×1380×220 μm. (b) Connection scheme of a quartz tuning fork for a cut perpendicular to the prongs. Adapted from Ref. [17] without permission.

detection today is based on microfabricated quartz tuning forks [16] which were originally developed for time-standards in quartz watches.

Fig. 7.5 (a) shows a photograph of a typical quartz tuning fork. It consists of a micro-machined quartz element shaped like a tuning fork with electrodes (right side) that are deposited on the surface of the device. At the base, the tuning-fork is supported by an epoxy mounting (left side). The overall length of the element without mount is about 5.87 mm. The width is 1.38 mm and the thickness of the element is 220 μm. It has two electric connections that contact the electrodes of the tuning fork element as sketched in Fig. 7.5 (b). For use in clocks and watches, the tuning-fork is encapsulated by a metal capsule in order to protect the tuning-fork against ambient parameters such as humidity and other potential deposits. The metal capsule has to be removed if the tuning-fork is to be used as a shear-force sensor. Tuning-fork crystals are fabricated in different sizes and different resonance frequencies. Most common frequencies are 2^{15} Hz = 32768 Hz and 100 kHz, respectively.

The mechanical oscillation of the tuning-fork prongs induces surface charges that are picked up by the electrodes and measured by an external electronic circuit. Hence, the tuning-fork acts as a mechanical-electrical converter, similar to a piezoceramic actuators. Vice versa, an alternating voltage applied to the tuning-fork electrodes gives rise to a mechanical oscillation of the prongs. The particular electrode layout on the tuning-fork ensures that only movements of the prongs against each other can be excited and detected electronically. This is because contraction and dilatation occurs perpendicular to the field lines sketched in Fig. 7.5 (b). If the tuning fork oscillation is excited via mechanical coupling to a separate oscillator (e.g. a piezo element) one has to make sure that the correct mode is excited because otherwise no signal can be detected. The advantages of quartz tuning forks compared to other piezoelectric elements apart from their small size are their standardized properties and low price due to large-scale production. The small size allows optical (fiber) probes to be attached to one prong of a fork such that even a weak interaction of the probe apex with the

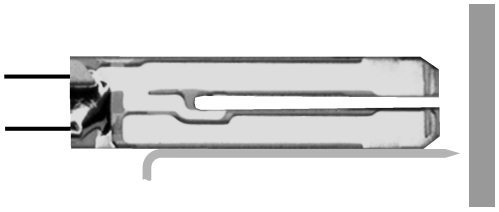

Figure 7.6: Cartoon of a quartz tuning fork sensor with attached tapered glass fiber (to scale) showing the relative dimensions of fiber probe and tuning fork sensor. Left: sensor. Right: sample.

sample will rigidly couple to the motion of the tuning fork element and influence its oscillation. Fig. 7.6 shows a sketch of a typical setting. In this scheme of shear-force detection, the tuning-fork prongs act as oscillating beams and not the probe itself. It is important that the probe itself does not oscillate at the frequency of the tuning-fork in order to prevent a coupled-oscillator type of operation. Hence, the length of the probe protruding from the tuning-fork end has to be kept as short as possible. For at ≈ 32 kHz tuning fork with an attached glass fiber probe, Eq. 7.1 implies that the protruding fiber lengths needs to be shorter than $\sim$2.3 mm.

7.1.3 The effective harmonic oscillator model

For small oscillation amplitudes $x(t)$ of the driven tuning-fork oscillation, the equation of motion for one prong of the tuning-fork is an effective harmonic oscillator

$$m\,\ddot{x}(d,t) \;+\; m\,\gamma(d)\,\dot{x}(d,t) \;+\; m\,\omega_{\rm o}^2(d)\,x(d,t) \;=\; F\,{\rm e}^{-i\omega t}\;. \tag{7.2}$$

Here, γ is the damping constant, $f_o \,=\, \omega_{\rm o}\,/\,2\pi$ the resonance frequency, and F a constant driving force which is, for example, supplied by an external dither piezo shaking the tuning-fork. The parameter d indicates the dependence on probe-sample distance. For ease of notation, the explicit dependence on d will be suppressed. The steady-state solution of Eq. (7.2) is

$$x(t) = \frac{(F/m)}{\omega_o^2 - \omega^2 - i\gamma\omega}\,{\rm e}^{-i\omega t}\;. \tag{7.3}$$

The amplitude of this oscillation is a Lorentzian lineshape function with a Q-factor

$$Q \;=\; \frac{f_o}{\Delta f} = \frac{\omega_o}{\gamma\,\sqrt{3}} \tag{7.4}$$

where Δf is the full-width at half-maximum (FWHM) of the resonance. Similar to γ and ω_o, the Q-factor and the oscillation amplitude $x(t)$ depends on the probe-sample distance d [see Fig. 7.3 (a)]. The Q-factor of a tuning-fork is in the order of $10^3 - 10^4$ at ambient conditions and can be several orders of magnitude higher at ultralow temperatures. Such a high Q originates from the fact that there is no center-of-mass motion. While one prong moves to the left, the other prong moves to the right so there is no net mass displacement.

The interaction of the probe with the sample surface affects two types of forces: (1) a dissipative friction-force associated with the second term in Eq. (7.2) and (2) a reactive elastic force due to the third term in in Eq. (7.2). We will derive expressions for both of these forces and estimate their magnitude. Let us first note that both, the damping constant γ and the spring constant $k = m\omega_o^2$ have two different constributions: (1) a static or intrinsic one associated with the physical properties of

the tuning-fork itself, and (2) an interaction-mediated contribution due to the probe-sample interaction. An expression for the interaction part of γ can be derived from the oscillation amplitude Eq. (7.3) evaluated at the resonance frequency, i.e.

$$\gamma(d) = \gamma_{stat} + \gamma_{int}(d) = \frac{(F/m)}{\omega_o(d)\, x_o(d)} \; . \tag{7.5}$$

with x_o being the oscillation amplitude and γ_{int} the interaction-mediated damping constant. Notice that $\gamma_{int}(d \rightarrow \infty) = 0$ which implies that

$$\gamma_{int}(d) = \gamma_{stat} \left[\frac{\omega_o(\infty)\, x_o(\infty)}{\omega_o(d)\, x_o(d)} \; - \; 1 \right] \; . \tag{7.6}$$

According to the second term in Eq. (7.2), the amplitude of the interaction induced friction force is calculated as

$$F_{int}^{friction}(d) \; = \; m\, \gamma_{int}(d)\, \omega_o(d)\, x_o(d) \; = \; \left[1 - \frac{\omega_o(d)\, x_o(d)}{\omega_o(\infty)\, x_o(\infty)} \right] \frac{k_{stat}\, x_o(\infty)}{\sqrt{3}\, Q(\infty)} \; . \tag{7.7}$$

where we used Eq. (7.4) and the property $m = k_{stat}/\omega_o^2(\infty)$. Next, we use the fact that the amplitude x_o changes faster with distance than the resonance frequency ω_o which allows us to drop the dependence on ω_o in the expression inside the brackets. Furthermore, the voltage V due to the induced surface charge at the surface of the tuning-fork is directly proportional to the oscillation amplitude and thus

$$F_{int}^{friction}(d) = \left[1 \; - \; \frac{V(d)}{V(\infty)} \right] \frac{k_{stat}}{\sqrt{3}\, Q(\infty)} x_o(\infty) \; . \tag{7.8}$$

This is they key expression for estimating the friction forces in shear-force microscopy. All the parameters in this expression are directly accessible. It can be shown that the ratio x_o/Q is independent of the probe-sample distance d which supports a viscous origin of the friction force, i.e. friction is proportional to velocity [5]. Thus, as the probe is approached towards the sample surface a reduction in oscillation amplitude corresponds to a proportional reduction of the quality factor.

Let us now work out the numbers for a realistic situation. The expression in brackets takes on the value of 0.1 if we assume a feedback setpoint corresponding to 90% of the original voltage $V(\infty)$. A 32 kHz tuning-fork with spring constant $k_{stat} = 40$ kN/m can be operated at an oscillation amplitude of $x_o(\infty) = 10$ pm (less than a Bohr radius !), and a typical quality factor with attached tip is $Q(\infty) \approx 1200$. With these parameters, the interaction-induced friction force turns out to be $F_{int}^{friction} \approx 20$ pN which is comparable with AFM measurements using ultrasoft cantilevers.

If a tuning-fork prong with $k_{stat} = 40$ kN/m is displaced by an amount of $x_o(\infty) = 10$ pm a surface charge difference of roughly ≈ 1000 electrons is build up between the two electrodes. Typically, the piezo-electromechanical coupling constant is in the order of

$$\alpha \; = \; 10\, \mu C/m \; . \tag{7.9}$$

The exact value depends on the specific type of tuning-fork. For an oscillation with 32 kHz, this corresponds to a current-to-displacement conversion of 2 A/m which has been confirmed experimentally with a laser interferometric technique [21]. Using a current-to-voltage conversion with a 10 MΩ resistance, an oscillation amplitude of $x_o(\infty) = 10$ pm gives rise to an oscillating voltage with amplitude $V = 200$ μV. This voltage must be further amplified before it is processed, for example, by a lock-in amplifier. While an oscillation amplitude of 10 pm seems to be very small it is nevertheless more than a factor of 20 larger than the thermally induced oscillation amplitude. The latter is calculated with help of the equipartition principle as

$$\frac{1}{2}k_{stat}x_{rms}^2 \;=\; \frac{1}{2}k_BT\;, \tag{7.10}$$

where T is the temperature and k_B the Boltzmann constant. At room temperature we obtain $x_{rms} = 0.32$ pm which corresponds to a peak noise amplitude of 0.45 pm.

Finally, we turn our attention to the elastic force associated with the third term in Eq. (7.2). Similar to the case of the damping constant, the spring constant k is characterized by a static and an interaction-induced part. Because the mass m is independent of the probe-sample proximity we obtain

$$m \;=\; \frac{k_{stat}+k_{int}(d)}{\omega_o^2(d)} \;=\; \frac{k_{stat}}{\omega_o^2(\infty)} \quad\rightarrow\quad k_{int}(d) = k_{stat}\left[\frac{\omega_o^2(d)}{\omega_o^2(\infty)} \;-\; 1\right]\;. \tag{7.11}$$

Introducing this relationship into the expression for the amplitude of the interaction-induced elastic force gives

$$F_{int}^{elastic}(d) = k_{int}(d)\,x_o(d) \;=\; \left[\frac{\omega_o^2(d)}{\omega_o^2(\infty)} \;-\; 1\right]\,k_{stat}\,x_o(d)\;. \tag{7.12}$$

As an example, we consider a small frequency-shift of 5 Hz and assume that this shift is again associated with a reduction of the oscillation amplitude $x_o(\infty) = 10$ pm to 90%, so that $x_o(d) = 9$ pm. For the same parameters as used before the elastic force amplitude turns out to be $F_{int}^{elastic} \approx 110$ pN which demonstrates that typically the elastic force is stronger than the friction force. However, as will be discussed later on, measurements of $F_{int}^{friction}$ rely on measurements of amplitude variations which is inherently slow for high Q-factors. Therefore, measurements of frequency shifts and thus of $F_{int}^{elastic}$ are often a good compromise between sensitivity and speed.

7.1.4 Response time

The higher the Q-factor of a system is the longer it takes to respond to an external signal. On the other hand, a high Q-factor is a prerequisite for high sensitivity. Thus, short response time and high sensitivity tend to counteract each other and a compromise has to be found between the two. The parameters of a tuning-fork used

for probe-sample distance control have to be adjusted so there is sufficient sensitivity to prevent probe or sample damage and that the response-time is sufficiently short to guarantee reasonable scanning speeds. For example, the use of ductile gold tips as near-field probes demands interaction forces smaller than ≈ 200 pN. The same is true if soft biological tissue is to be imaged. Such small forces require a high Q-factor which limits the image acquisition time.

To illustrate the relationship between Q-factor and response time, let us consider the amplitude and phase of the complex steady-state solution of the harmonic oscillator model [c.f. Eq. (7.3)]

$$x_o = \frac{(F/m)}{\sqrt{(\omega_o^2 - \omega^2)^2 + \omega_o^2\omega^2 \,/\, 3Q^2}} \,, \tag{7.13}$$

$$\varphi_o = \tan^{-1}\left[\frac{\omega_o\omega}{\sqrt{3}Q\,(\omega_o^2 - \omega^2)}\right] \,. \tag{7.14}$$

where we replaced the damping constant in terms of the quality factor using Eq. (7.4). In terms of x_o and φ_o the solution can be written as

$$x(t) = x_o \cos\left(\omega t + \varphi_o\right) \,. \tag{7.15}$$

We will now consider what happens if the probe-sample distance d is abruptly changed from one value to another [9]. As an initial condition we assume that the resonance

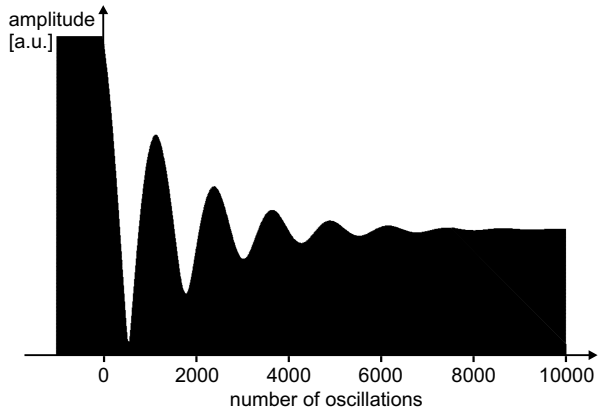

Figure 7.7: Transient response of a oscillating tuning fork (Q=2886) upon a change in probe-sample distance d at $t = 0$. The step causes a resonance frequency shift of 16.5 Hz from 33000 to 33016.5 Hz following Eq. (7.16). Only after $\sim 2Q$=10000 oscillation periods the new steady state is reached. Individual oscillations can not be resolved - only the envelope is visible.

frequency changes instantaneously from ω_o to ω'_o at the time $t = 0$. The solution is provided by Eq. 7.2, and with the proper boundary conditions we obtain

$$x(t) = x'_o \cos(\omega t + \varphi'_o) + x_t e^{-\omega'_o t/2\sqrt{3}Q} \cos(\omega_t t + \varphi_t) \ . \tag{7.16}$$

The solution consists of a steady-state term (left) and a transient term (right). x'_o and φ'_o are the new steady-state amplitude and phase, respectively. Similarly, x_t and φ_t and ω_t are the corresponding parameters of the transient term. Their exact values follow from the boundary conditions.

Fig. 7.7 shows the envelope of a typical transient behavior described by Eq. 7.16 for a tuning fork with a typical Q-factor of 2886. Upon a change of distance at $t = 0$ it takes about Q oscillation cycles to reach the new steady state. The response time of the tuning fork can be defined as

$$\tau = \frac{2\sqrt{3}Q}{\omega'_o} \approx \frac{2\sqrt{3}Q}{\omega_o} \ , \tag{7.17}$$

which is as large as ∼300 ms. Thus, the bandwidth of the feedback loop becomes very small and the scanning speeds very slow if the amplitude serves as a feedback signal. To overcome this problem, it was proposed to use the resonance frequency shift as a feedback signal [9]. In first approximation, the resonance frequency responds instantaneously to a perturbation, however, one has to keep in mind that it takes at least one oscillation period to define a frequency. The frequency shift can be monitored, for example, by using a phase-locked loop (PLL) similar to FM demodulators used in radios. However, also here the available bandwidth is not unlimited because of low pass filtering used in the process. In other words, a number of oscillation cycles are necessary to compare the phase to be measured with a reference.

7.1.5 Equivalent electric circuit

So far, we have assumed that the tuning-fork is driven by a constant driving force F. This force can be supplied mechanically by an external dither piezo attached in the vicinity of the tuning fork. This type of mechanical excitation is favorable from a point of view that the driving circuit is electrically decoupled from the system and hence provides better stability and noise-performance. On the other hand, mechanical shaking gives rise to center-of-mass oscillation of the tuning-fork which does not correspond to the desired 'asymmetric' mode of operation (prongs oscillating out of phase). Consequently, mechanical excitation provides poor coupling to the tuning-fork oscillation. Electrical excitation can be more favorable because of the simplicity of implementation. When using the fully electric operation of a tuning-fork the measurement of the dither motion reduces to a simple impedance $Z(\omega)$ or admittance $Y(\omega)$ measurement.

The admittance of a piezoelectric resonator can be modelled by a Butterworth-Van-Dyke equivalent circuit [17] as shown in Fig. 7.8 (a). It can be expressed as

$$Y(\omega) = \frac{1}{Z(\omega)} = \frac{1}{R + (i\omega C)^{-1} + i\omega L} + i\omega C_0 \quad . \tag{7.18}$$

Here, the inductance L, the resistance R, and the capacitance C are characteristic values for a certain type of resonator. The parallel capacitance C_0 originates from the pick-up electrodes and external leads connecting to the resonator. Eq. 7.18 can be represented by a Nyquist plot [see Fig. 7.9 (a)] where $Im(Y)$ is plotted against $Re(Y)$ parameterized by the frequency ω. The resulting plot, characteristically for a resonator, is a circle in the complex plane which is offset along the imaginary axis by ωC_0. Plotting the absolute value of $Y(\omega)$ as a function of ω yields the resonance curve of the oscillator shown in Fig. 7.9 (b) using a logarithmic scale. Using the parameters of a typical tuning-fork listed in the caption of Fig. 7.9 gives rise to a resonance at 32765 Hz. The resonance frequency is determined by $f_o = 1/(2\pi\sqrt{LC})$ and the quality factor by $Q = \sqrt{L/(CR^2)}$. The small negative peak at higher frequencies is a consequence of the stray capacitance C_0 as it can be traced back to the offset in the circular admittance locus in Fig. 7.9 (a). Increasing C_0 does hardly influence the position of the resonance peak but it distorts the shape of the curve by moving the second peak closer to the actual resonance.

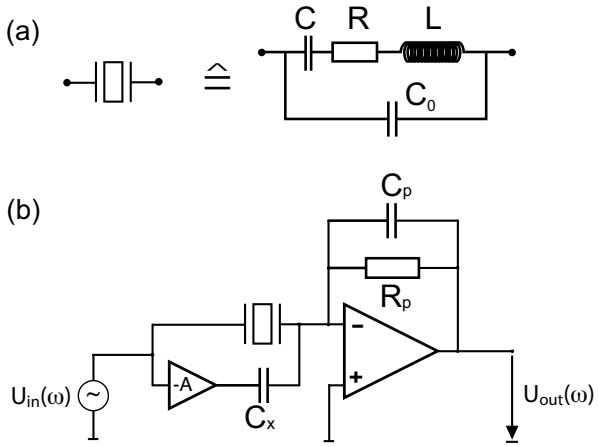

Figure 7.8: Equivalent electric circuit of a tuning-fork and its measurement. (a) Symbol and Butterworth-Van-Dyke equivalent circuit. (b) Measurement of the tuning-fork admittance. The capacitor C_x and the gain of $-A$ compensate for the tuning-fork's stray capacitance C_0.

A scheme for measuring the admittance is depicted in Fig. 7.8 (b). The transfer function of this circuit is determined as

$$\frac{U_{out}}{U_{in}}(\omega) = -\frac{R_p}{1+i\omega R_p C_p}\,\frac{\left[i\omega C + (1-\omega^2 CL + i\omega RC)(i\omega C_0 - Ai\omega C_x)\right]}{1-\omega^2 CL + i\omega RC} \quad . \tag{7.19}$$

It can be seen that by adjusting the variable negative gain $-A$ it is possible to compensate for the influence of C_0 which, if left uncompensated, results in a suboptimal signal-to noise ratio due to the high and low frequency offset introduced to U_{out}. The first term in Eq. (7.19) corresponds to a low-pass filter due to the feedback resistor's stray resistance. Notice, that the current through the tuning-fork is directly determined by the applied voltage U_{in}. Thus, following our previous example, an interaction-induced friction force of $F_{int}^{friction} = 20$ pN (10 pm oscillation amplitude) requires an input voltage of $U_{in} \approx 200$ μV. Such a small voltage is difficult to deliver and requires voltage dividers close to the tuning-fork circuit if a reasonable signal-to-noise ratio is to be achieved. From this perspective, mechanical excitation can be favorable over electrical excitation. Finally, it should be noted that the piezo-electromechanical coupling constant α [c.f. Eq. (7.9)] can be determined if both the mechanical constants and the equivalent electrical constants of the tuning-fork are known [17]. For example, by equating the potential energies $Q^2/2C = k_{stat}x_o^2/2$ and replacing the charge Q by αx_o one finds

$$\alpha \;=\; \sqrt{k_{stat}\,C} \quad . \tag{7.20}$$

Similar relationships can be derived by considering the equivalence of kinetic energies.

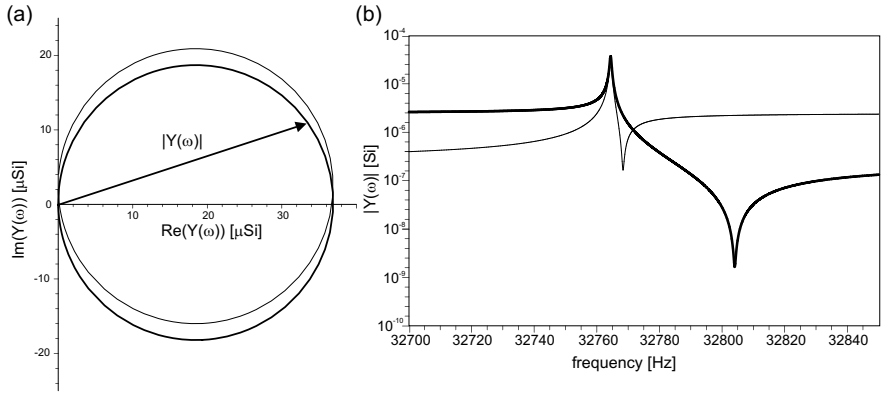

Figure 7.9: Plots of the admittance $Y(\omega)$. (a) Nyquist plot of the admittance in the complex plane. The values used for the plot are C_0=1.2 pF, L=8.1365 kH, R=27.1 kΩ, and C=2.9 fF. For the thin line the stray capacitance was increased by a factor of ten. (b) Absolute value of the admittance as a function of the frequency of the applied voltage $U(\omega)$.

7.2 Normal force methods

Using shear-force interactions to control the probe-sample distance has the advantage that any type of probe tip can be used as long as it is approximately shaped like a pencil and is small enough to be attached to a tuning fork. The disadvantage of this configuration is that the spring constant of the probe normal to the surface is very high. This means that a small instability or even the unavoidable small error in probe-sample distance control (as it might occur at steep steps in the sample) is immediately translated into a very high normal force acting on the probe apex. Thus, shear-force feedback is a risky operation if there is little information on surface topology. In AFM, this problem is less important since commercial AFM cantilevers have a well-defined and rather small spring constants normal to the probing tip. As a consequence, small instabilities result in only small excess forces acting on the probe apex. For these reasons, and with the goal of mass production, integration, and user friendliness in mind, there have been several attempts to integrate near-field probes on to AFM cantilevers. In the following, we will discuss two different implementations working in normal mode operation.

7.2.1 Tuning fork in tapping mode

By using the arrangement shown in Fig. 7.10 a probe attached to a tuning fork can also be operated in tapping mode. For optical fibers it was found to be necessary to break the fiber just above the fixation point on the tuning fork to allow for a free vibration of the prong [22]. Light is then delivered via a second cleaved fiber that is positioned just above the probe fiber. In normal force operation, the attached fiber probe is allowed to protrude several millimeters beyond the attachment point because the normal motion is not able to excite fiber vibration. For example, the protruding

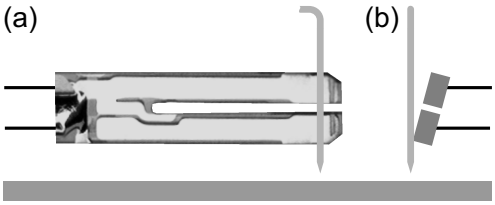

Figure 7.10: Tuning fork operated in tapping mode. The tuning fork is aligned parallel to the sample while the probe is oscillating perpendicular. (a) Side view, (b) Front view. The fork is slightly tilted in order not to affect the second arm.

fiber can be dipped into a liquid cell without wetting the tuning fork which is very favorable for biological imaging. Also, since tuning fork prongs are very stiff cantilevers they can be used for noncontact AFM in UHV since snap-into-contact does appear only at very small probe-sample distances [23].

7.2.2 Bent fiber probes

Cantilevered aperture probes with reasonably soft spring constants can be created by deforming standard fiber probes during the fabrication process using a CO_2-laser. The fiber is aligned parallel to the sample surface with the bent fiber-end facing the sample perpendicularly. During raster-scanning, the vertical motion of the fiber can be read out by standard AFM beam deflection techniques. Fig. 7.11 shows a selection of cantilevered fiber probes found in the literature. Because of their soft spring constants and the good Q-factors, bent fiber probes have been used for imaging of soft samples under liquids, see e.g. [24, 25].

7.3 Topographic artifacts

In any type of scanning probe microscopy, image formation relies on recording a strongly distance dependent physical interaction between probe and sample. The information encoded in the recorded images depends on the tip shape and on the path

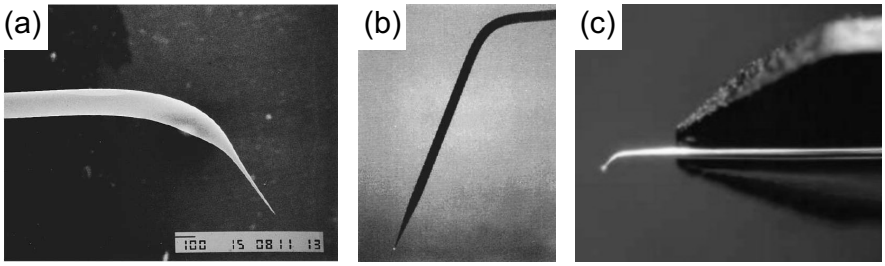

Figure 7.11: Cantilevered fiber probes. (a) Bent fiber probe with a mirror facet for beam deflection. The resonant frequency of the cantilevered probe is ∼14 kHz and the Q factor is ∼30 in water sufficient to perform near-field imaging on soft samples in liquid cells. From Ref. [24] without permission. (b) Different type of bent fiber probe. The resonances are typically in the range of 30 to 60 kHz, the Q factors are larger than 100, and the measured spring constants are 300 to 400 N/m. From Ref. [25] without permission. (c) Commercially available cantilevered fiber probe from Nanonics. Without permission.

the tip takes. In AFM, for example, non-ideal tip shapes are an important source for misinterpretations. Blunt tips lead to low-pass filtered images, i.e., deep and narrow trenches cannot be recorded because the tip doesn't fit in (see e.g. [26]). In some scanning probe techniques a single tip is capable of measuring several interactions simultaneously. For example, AFM can record force and friction by simultaneously measuring cantilever bending and torsion. However, only one of these measurements can be used as a feedback signal for controlling the probe-sample distance. While the feedback keeps one signal constant it can introduce artifacts to the other signal. For example, as the shear-force feedback in a near-field optical microscope adjusts for a distance change, the vertical motion of the optical probe can lead to intensity variations that are not related to the optical properties of the sample. In this section we will analyze potential artifacts in near-field optical imaging that arise from the fact that the optical signal is an auxiliary signal not used in the feedback loop.

Let us denote by X the distance-dependent *feedback signal* originating from a specific probe-sample interaction such as shear-force or normal force. The respective X-image will reflect the piezo movements that were necessary to keep X constant during scanning. All other signals are *auxiliary signals* that result from the boundary condition X=constant. In principle, any distance dependent signal can serve as the feedback signal. It has, however, to fulfill the following conditions: (1) The probe–sample distance dependence must be short-ranged in order to maintain the probe in close proximity to the sample and thus to guarantee high resolution, and (2) the distance dependence must be a piecewise monotonous function to guarantee a stable feedback loop. Typically, a near-field optical microscope renders two simultaneously recorded images: (1) a topographic image originating from keeping the shear-force feedback signal constant, and (2) an optical near-field image due to spatially varying optical properties of the sample and due to probe-sample distance variations. The optical image can result, for example, from local variations of sample transmission or from spatially distributed fluorescent centers.

In most cases, the optical interaction is not suitable as a feedback signal because it is neither short–ranged nor monotonously dependent on probe-sample distance. For example, the optical transmission of an aperture probe near a transparent substrate was discussed in chapter 6. If the emission is integrated over a large range of angles that covers also angles larger than the critical angle of the substrate, an increase of the transmission for small distances is observed. For larger distances, however, interference undulations render the optical response non-monotonous. Furthermore, the local light transmission could be completely suppressed when the probe is scanned over a metal patch. This would result in a loss of the feedback signal in an unpredictable way. As a consequence, optical signals are recorded under the condition that the shear force interaction is maintained constant. This condition can be responsible for topographic artifacts in the near-field optical signal.

A representative sample with large topographic variations is depicted in Fig. 7.12. It exhibits uniform optical properties but its topographic features are large compared with the overall shape of the optical probe. From the discussion in chapter 6 we know that aperture probes have a more or less conical shape with a flat facet at the apex. For the following we assume that the short-range probe-sample distance dependence of the optical signal decreases monotonously. This is reasonable because of the confined and enhanced fields near the aperture. The topography of the sample (S) is assumed to be measured via shear force feedback and, as the probe's profile is not a delta function, the measured profile (T) will always differ from the actual sample profile (S). The 'mechnical' point of contact changes during scanning and gives rise to variations in the 'optical' probe-sample distance. The optical latter can be defined as the vertical distance between the center of the aperture and the sample profile (S). As the optical signal is distance–dependent, it will reflect differences between (S) and (T). The resulting optical signal is sketched in Fig. 7.12, trace (O). It demonstrates the appearance of features in the optical image purely related to a topographic artifact.

A second limiting case is a sample with uniform optical properties with topographic features that are small compared with the overall shape of the probe (see Fig. 7.13). The end of an aperture probe is typically not smooth but exhibits grains that result from the metal evaporation process [c. f. Fig. 6.22]. These grains often act as mini-tips that mediate the shear force interaction. Here we assume that a single mini-tip is active. Because of the mini-tip, the apparent topography (T) will match the actual topography (S) very well. The probe produces an excellent high-resolution topographic image. However, while scanning over the small features of the sample (S) in force feedback, the average distance between optical probe (OS) and sample surface will change because of the distance-dependent optical signal. This leads to an optical image that contains small features highly correlated to the topography. In particular,

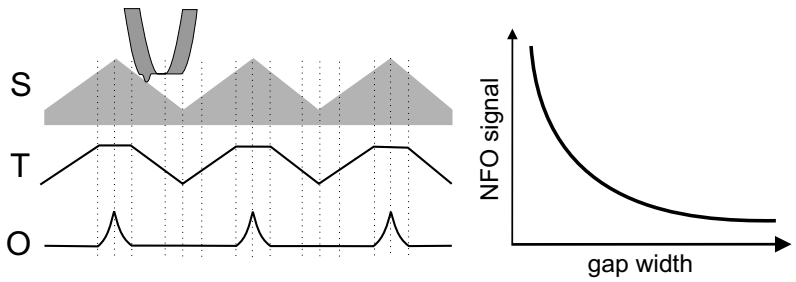

Figure 7.12: Near-field optical imaging on a sample with large topographic variations. Left panel: S: sample profile, T: apparent topography measured by the tip, O: detected optical signal resulting from the particular probe-sample distance dependence (right panel).

it is possible that the size of these optical features turns out to be *much smaller* than what could be expected from the available optical resolution, e.g. estimated from the aperture diameter of the optical probe determined independently by SEM.

7.3.1 Phenomenological theory of artifacts

In order to put the discussion on a more solid ground, we introduce system signal functions $S_{\rm NFO}(x,y,z)$ and $S_{\rm SF}(x,y,z)$ which represent the optical signal and the distance-dependent feedback signal, respectively [3]. Both signals depend on the coordinates (x,y,z) of the probe relative to the sample. The signal $S_{\rm NFO}$ can represent, for example, the locally transmitted or reflected light, polarized or depolarized components of locally scattered light, or the fluorescence due to local excitation by the near-field probe. $S_{\rm NFO}$ can also be the amplitude or phase of a modulated signal if differential techniques such as probe dithering are employed. Typically, $S_{\rm NFO}$ exhibits a weaker probe-sample distance dependence compared with the feedback signal $S_{\rm SF}$.

The signals that are actually recorded during an experiment can be derived from $S_{\rm NFO}(x,y,z)$ and $S_{\rm SF}(x,y,z)$ by specifying a path that the probe takes. This path depends on the mode of operation of the microscope. Let these recorded signals be $R_{\rm NFO}(x,y)$ and $R_{\rm SF}(x,y)$ where

$$R_{\rm NFO}(x,y) = S_{\rm NFO}[x,y,z_{\rm scan}(x,y)] \tag{7.21}$$

$$R_{\rm SF}(x,y) = S_{\rm SF}[x,y,z_{\rm scan}(x,y)] \ . \tag{7.22}$$

Here, $z_{\rm scan}(x,y)$ is the path of the probe. It can be derived from the voltage applied to the distance-controlling piezo element. The relation between the different signals is illustrated in Fig. 7.14.

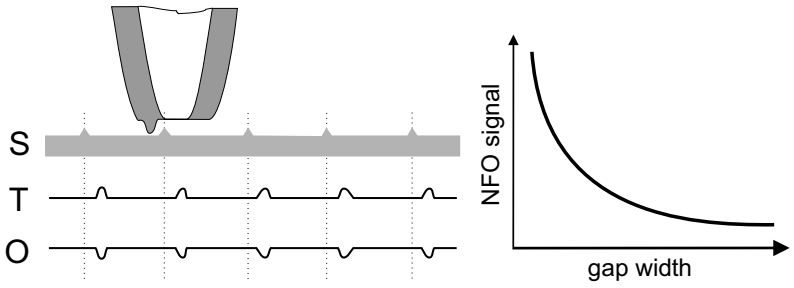

Figure 7.13: Near-field optical imaging on a sample with small topographic variations: (S) sample profile, (T) apparent topography as measured by the probe, (O) detected optical signal resulting from the particular probe-sample distance dependence (right panel).

Constant height mode

In constant-height mode, the probe is scanned in a plane parallel to the average object surface, resulting in

$$z_{\mathrm{scan}} = z_{\mathrm{set}} \tag{7.23}$$

$$R_{\mathrm{NFO}}(x,y) = \overline{S}_{\mathrm{NFO}}(z_{\mathrm{set}}) + \delta S_{\mathrm{NFO}}(x,y,z_{\mathrm{set}}) \quad , \tag{7.24}$$

where we separated a constant background $\overline{S}_{\mathrm{NFO}}$ form the signal. Any structure visible in the scan image corresponds to a lateral variation of S_{NFO} originating from *optical* or surface related properties of the sample.

Constant gapwidth mode

In constant gapwidth mode, the feedback forces the probe to follow a path of (nearly) constant probe-sample separation. Consequently,

$$R_{\mathrm{SF}}(x,y) = S_{\mathrm{SF}}(x,y;z_{\mathrm{scan}}) \approx R_{\mathrm{set}} \tag{7.25}$$

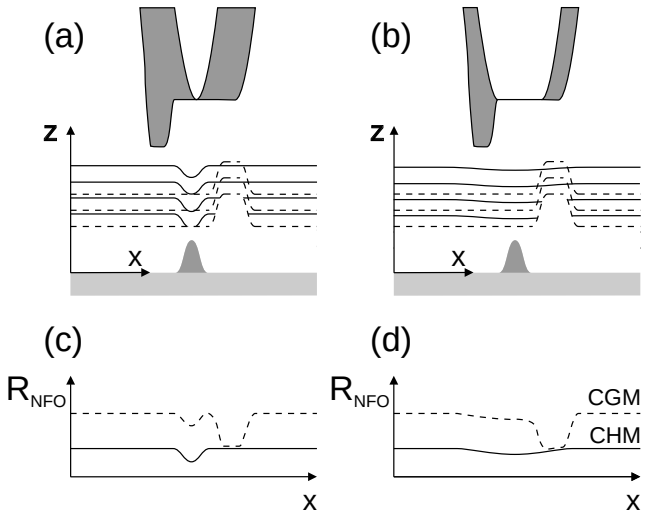

Figure 7.14: Influence of probe geometry on recorded scan images. The near-field signal S_{NFO} is represented by solid lines and the feedback signal S_{SF} by dashed lines. Both scan-lines are plotted relative to the center of the aperture probe. The mini-tip on the rim of the aperture is oversized to better visualize the resulting effects. (c,d) Recorded scan-lines for different modes of operation: constant-gapwidth mode (CGM) and constant-height mode (CHM). CGM introduces artifacts because of the varying probe-sample distance. From [3].

$$z_{\text{scan}} = \overline{z} + \delta z(x,y) \tag{7.26}$$

$$R_{\text{NFO}}(x,y) = \overline{S}_{\text{NFO}}(\overline{z}) + \delta S_{\text{NFO}}(x,y,\overline{z}) + \frac{\partial S_{\text{NFO}}}{\partial z}\Big|_{\overline{z}} \cdot \delta z \ . \tag{7.27}$$

In Eq. (7.25) the $\approx$ symbol indicates possible deviations caused by technical limitations of the electro-mechanical feedback circuit. Such deviations can become significant when the topography undergoes rapid changes and/or the scan speed is too high. Furthermore, $\overline{z}$ is the average z-position of the probe, and $\delta z(x,y)$ describes the variations of the z-position around $\overline{z}$ due to the feedback. It should be emphasized that the following considerations are valid for any path that the probe may take, no matter whether it follows the topography exactly or not.

The signal $R_{\text{NFO}}(x,y)$ in Eq. (7.27) is developed into a power series of δz of which only the first terms are retained. The first two terms render the same signal as obtained under constant-height mode operation. However, the third term represents the coupling of the vertical z motion with the optical signal. It is this term that leads to common artifacts. For the optical properties to dominate, the variations of light intensity in a scan image have to satisfy

$$\delta S_{\text{NFO}}(x,y;\overline{z}) \gg \frac{\partial S_{\text{NFO}}}{\partial z}\Big|_{\overline{z}} \cdot \delta z \ . \tag{7.28}$$

This condition becomes more difficult to achieve the stronger the light confinement of the optical probe is. This is because a laterally confined field decays very rapidly with distance from the probe. Therefore, probe-sample distance variations have a much stronger effect and can easily overshadow any contrast originating from the optical properties of the sample.

For two different probes, Figs. 7.14(c,d) show the signals that are recorded in constant-height mode and in constant-gapwidth mode. Only the probe with the small aperture provides an optical image representative of the sample. The large aperture probe cannot generate any high-resolution optical image, and in constant-gapwidth mode operation, the scan lines are dominated by the shear-force response specific to the passage over the bump. In Fig. 7.14(c), the true near-field signal can still be recognized but in Fig. 7.14(d) the CGM trace is not at all related to the optical properties of the sample.

7.3.2 Example of near-field artifacts

A simple experiment shall serve as an illustration of artifacts originating from different modes of operation. Fig. 7.15 shows topographic images and near-field optical transmission-mode images of a so-called Fischer projection pattern [29]. Such patterns are created by evaporating a thin layer of metal onto a closely packed monolayer of latex spheres. The triangular voids between the spheres are filled with metal.

After metal evaporation, the latex spheres are washed away in an ultrasonic bath. The result is a sample with periodically arranged triangular patches. These patches, when imaged at close proximity show strong optical absorption contrast. The process of using microspheres for creating nanostructured surfaces is also called *nanosphere lithography*.

The same sample was imaged using two different aperture probes: (1) a probe with an aperture on the order of 50 nm (good probe) and (2) a probe with a large aperture of 200 nm (bad probe). Because the metal patches are created using 200 nm spheres, the resulting triangular patches have a characteristic size of about 50 nm which can only be resolved using the good probe. For both probes, two sets of images were recorded: one in constant-gapwidth mode using shear-force feedback, and one in constant-height mode. The left panel shows the results for the good probe: in constant-gapwidth mode the topography of the sample is well reproduced probably due to a minitip on the aperture. The optical image strongly resembles the topographic image. It is difficult to tell how much the optical signal is influenced by the feedback. When the same area is imaged using constant-height mode (lower left row), the topographic signal is constant apart from isolated spots where the feedback becomes activated to prevent the probe from touching the surface (white spots).

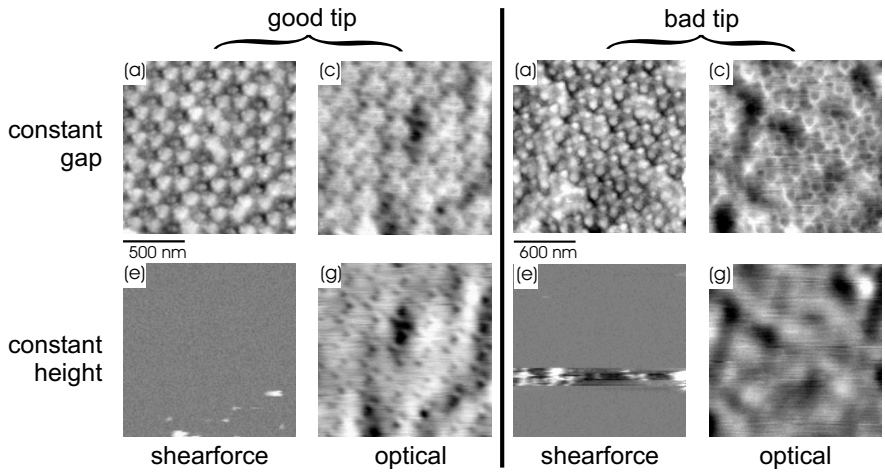

Figure 7.15: Imaging of a latex sphere projection pattern in constant-gapwidth mode (upper row) and constant-height mode (lower row) with two different near-field probes, a 'good' probe with an aperture of 50 nm (left side) and a 'bad' probe with an aperture of 200 nm (right side). The constant gapwidth topographic and optical images show sharp features for both tips but only the constant-height mode image for the 'good' tip shows optical contrast.

However, the optical signal completely changes its appearance. The contrast becomes much clearer and the metal patches are well-resolved. For the bad probe, we observe an optical image with fine details only in constant-gapwidth mode. As soon as we switch to constant-height mode the optical resolution becomes much worse. This shows clearly that the apparent optical resolution observed in the constant gapwidth optical image is purely artificially induced by the feedback loop.

7.3.3 Discussion

We have determined that if a force feedback is applied to control the probe-sample distance it is not possible to record near-field images with pure optical contrast of samples with structured surfaces. Images recorded in the constant height mode are more likely to reflect the true optical resolution and contrast. Constant height imaging does not use feedback control while scanning. The probe is raster-scanned in a plane parallel to the mean sample surface. The measured optical signal can thus not be influenced by feedback movements of the tip. Although constant height images are more likely to represent the optical properties of the sample, they are still subject to misinterpretations because of the varying distance between probe and sample when scanning over structured surfaces. *Real* optical contrast can only be expected if the aperture size is sufficiently small compared with the characteristic size of sample features and if the local optical coupling between probe and sample is large. Although the contrast originating from a varying probe-sample distance is a purely topographic effect it should not be considered an artifact but a property inherent to near-field optical imaging. As the minimum distance between probe and sample is given by the highest topographic feature within the scan range, high resolution can only be expected on samples with low topography. Features on the bottom of surface depressions will be poorly resolved. In short, only features interacting with the highly localized near-field of the optical probe can be imaged with high resolution.

Image interpretation can be greatly facilitated by taking spectroscopic information into account. For example, the spectrum of fluorescence emission can define the nature of the emitting fluorophore (e.g. chlorophyll in photosynthetic membranes) and Raman spectra provide a highly specific fingerprint for the chemical composition of the sample (e.g. structure of a carbon nanotube). Thus, near-field optical imaging combined with spectroscopy is able to unambiguously localize certain target molecules. Consequently, the recorded images are artifact-free maps of the spatial distribution of the target species. Despite of this clear advantage, varying probe-sample distances will still pose a problem for quantifying the local concentration of the target species. In any case, spectroscopic near-field imaging provides a clear advantage over near-field absorption or scattering measurements because the recorded signal is a strongly material specific signature.

Problems

Problem 7.1 In tip-enhanced microscopy, a pointed gold wire is attached to one arm of a tuning-fork. Assume that the wire is cylindrical with a diameter of 100 μm and that the tuning-fork's resonance frequency is 32.7 kHz. In order that the attached gold wire follows the oscillation of the tuning-fork more or less instantaneously, the resonance frequency of the protruding wire must be at least twice the tuning-fork frequency. Determine the maximum length of the protruding wire.

Problem 7.2 With the help of the equipartition principle we determined the thermally activated oscillation x_{rms} of the tuning fork. Here we calculate the spectral force density $S_F(f)$ in units of N^2/Hz. S_F is the spectral noise force that excites the end of a tuning-fork prong to a vibration amplitude x_{rms}. It has a flat frequency dependence (white noise) and can be determined through

$$x_{rms}^2 \;=\; \int_0^\infty S_F \, \frac{f_o^2/k}{(f_o^2 - f^2) \,+\, i\, f f_o/Q} \, df \;.$$

Here, the Lorentzian term following S_F is the transfer function of the tuning-fork.

1. Determine S_F in terms of the spring constant k, the Q-factor Q, the temperature T, and the resonance frequency f_o.
   Hint: Evaluate the integral in the limit $Q \gg 1$ and apply the equipartition theorem.
2. Use $k = 40\,\mathrm{kN/m}$, $T = 300\,\mathrm{K}$, $f_o = 32.7\,\mathrm{kHz}$, and $Q = 1000$ to determine the thermal force in a spectral bandwidth of 100 Hz.

Problem 7.3 Due to the typically high Q-factor of a tuning fork it takes a long time for the oscillation amplitude to respond to a sudden change of the feedback signal.

1. Derive the solution given in Eq. (7.16) for a tuning-fork whose frequency changes abruptly from one frequency to another at the time $t = 0$. Determine the values of x_t, φ_t and ω_t.
2. Repeat the calculation but assume that the driving force F changes abruptly from one value to another at $t = 0$.
3. Discuss the main difference between the solutions in (1) and (2).

References

[1] G. Binnig and H. Rohrer. Scanning tunneling microscopy. *Helv. Phys. Acta* **55**, 726 (1982).

[2] G. Binnig, C. F. Quate, and C. Gerber. Atomic force microscope. *Phys. Rev. Lett.* **56**, 930–933 (1986).

[3] B. Hecht, H. Bielefeldt, L. Novotny, Y. Inouye, and D. W. Pohl. Facts and artifacts in near–field optical microscopy. *J. Appl. Phys.* **81**, 2492–2498 (1997).

[4] R. Carminati, A. Madrazo, M. Nieto-Vesperinas, and J.-J. Greffet. Optical content and resolution of near–field optical images: Influence of the operation mode. *J. Appl. Phys.* **82**, 501 (1997).

[5] K. Karrai and I. Tiemann, "Interfacial shear force microscopy," *Phys. Rev. B* **62**, 13 174–13 181 (2000).

[6] B. C. Stipe, H. J. Mamin, T. D. Stowe, T. W. Kenny, and D. Rugar, "Noncontact friction and force fluctuations between closely spaced bodies," *Phys. Rev. Lett.* **87**, 96 801 (2001).

[7] J.R. Zurita-Sánchez, J.-J. Greffet, and L. Novotny. Friction forces arising from fluctuating thermal fields. *Phys. Rev. A* **69**, 022902 2004.

[8] L. D. Landau and E. M. Lifshitz. *Theory of Elasticity.* Pergamon, Oxford (1986).

[9] T. R. Albrecht, P. Grütter, D. Horne, and D. Rugar. Frequency modulation detection using high-q cantilevers for enhanced force microscope sensitivity. *J. Appl. Phys.* **69**, 668 (1991).

[10] E. Betzig, P.L. Finn, and S.J. Weiner. Combined shear force and near-field scanning optical microscopy. *Appl. Phys. Lett.* **60**, 2484 (1992).

[11] R. Toledo-Crow, P.C. Yang, Y. Chen, and M. Vaez-Iravani. Near-field differential scanning optical microscope with atomic force regulation. *Appl. Phys. Lett.* **60**, 2957 (1992).

[12] D. Rugar, H. J. Mamin, and P. Guethner. Improved fiber–optic interferometer for atomic force microscopy. *Appl. Phys. Lett.* **55**, 2588 (1989).

[13] G. Tarrach, M.A. Bopp, D. Zeisel, and A.J. Meixner. Design and construction of a versatile scanning near–field optical microscope for fluorescence imaging of single molecules. *Rev. Sci. Instrum.* **66**, 3569–3575 (1995).

[14] J. Barenz, O. Hollricher, and O. Marti. An easy-to-use non-optical shear-force distance control for near-field optical microscopes. *Rev. Sci. Instrum.* **67**, 1912–1916 (1996).

[15] J.W.P. Hsu, M. Lee, and B.S. Deaver. A nonoptical tip-samle distance control method for near-field scanning optical microscopy using impedance changes in an electromechanical system. *Rev. Sci. Instrum.* **66**, 3177 (1995).

[16] K. Karrai and R.D. Grober. Piezoelectric tip-sample distance control for near field optical microscopes. *Appl. Phys. Lett.* **66**, 1842 (1995).

[17] J. Rychen, T. Ihn, P. Studerus, A. Herrmann, K. Ensslin, H.J. Hug, P.J.A. van Schendel, and H.J. Gntherodt. Operation characteristics of piezoelectric quartz tuning forks in high magnetic fields at liquid helium temperatures. *Rev. Sci. Instrum.* **71**, 1695–1697 (2000).

[18] A. Arnau, T. Sogorb, and Y. Jimenez. A continuous motional series resonant frequency monitoring circuit and a new method of determining butterworthvan dyke parameters of a quartz crystal microbalance in fluid media. *Rev. Sci. Instrum.* **71**, 2563–2571 (2000).

[19] A.G.T. Ruiter, J.A. Veerman, K.O. van der Werf, and N.F. van Hulst. Dynamic behavior of tuning fork shear-force feedback. *Appl. Phys. Lett.* **71**, 28–30 (1997).

[20] J. Rychen, T. Ihn, P. Studerus, A. Herrmann, and K. Ensslin. A low-temperature dynamic mode scanning force microscope operating in high magnetic fields. *Rev. Sci. Instrum.* **70**, 2765–2768 (1999).

[21] R.D. Grober, J. Acimovic, J. Schuck, D. Hessman, P.J. Kindlemann, J. Hespanha, A.S. Morse, K. Karrai, I. Tiemann, and S. Manus. Fundamental limits to force detection using quartz tuning forks. *Rev. Sci. Instrum.* **71**, 2776–2780 (2000).

[22] A. Naber, H.-J. Maas, K. Razavi, and U.C. Fischer. Dynamic force distance control suited to various probes for scanning near-field optical microscopy. *Rev. Sci. Instrum.* **70**, 3955–3961 (1999).

[23] F.J. Giessibl, S.Hembacher, H. Bielefeldt, and J. Mannhart. Subatomic features on the silicon (111)-(7x7) surface observed by atomic force microscopy. *Science* **289**, 422–425 (2000).

[24] H. Muramatsu, N. Chiba, , K. Homma, K. Nakajima, T. Ataka, S. Ohta, A. Kusumi, and M. Fujihira. Near–field optical microscopy in liquids. *Appl. Phys. Lett.* **66**, 3245 (1995).

[25] C.E. Talley, G.A. Cooksey, and R.C. Dunn. High resolution fluorescence imaging with cantilevered near-field fiber optic probes. *Appl. Phys. Lett.* **69**, 3809–3811 (1996).

[26] M. Hietschold, H. Sbosny, A. Bruska, and M. Röder. Scanning tunneling microscopy for geometrical measurement on the nanometer scale. *Proc. Quantitative Mikroskopie*, PTB–Bericht F–**21**, 80 (1995).

[27] D. Keller. Reconstruction of STM and AFM images distorted by finite–size tips. *Surf. Sci.* **253**, 353 (1991).

[28] K. Luo, Z. Shi, J. Lai, and A. Majumdar. Nanofabrication of sensors on cantilever probe tips for scanning multiprobe microscopy. *Appl. Phys. Lett.* **68**, 325 (1996).

[29] U.Ch. Fischer and H.P. Zingsheim. Submicroscopic pattern replication with visible light. *J. Vac. Sci. Technol.* **19**, 881–885 (1981).